Available online at www.sciencedirect.com

jmr&t
Journal of Materials Research and Technology

journal homepage: www.elsevier.com/locate/jmrt

Original Article

Surface enhancement of Ti–6Al–4V fabricated by selective laser melting on bone-like apatite formation

A.N. Aufa [a], Mohamad Zaki Hassan [a,*], Zarini Ismail [b], Norhaslinda Harun [c], James Ren [d], Mohd Faizal Sadali [a]

[a] Razak Faculty of Technology and Informatics, Universiti Teknologi Malaysia, Jalan Sultan Yahya Petra, 54100 Kuala Lumpur
[b] Faculty of Medicine and Health Sciences, Universiti Sains Islam Malaysia, Bandar Baru Nilai, 71800 Nilai, Negeri Sembilan
[c] Diploma Programme Space, Universiti Teknologi Malaysia, Jalan Sultan Yahya Petra, 54100 Kuala Lumpur
[d] School of Engineering, Liverpool John Moores University, James Parson Building, Byrom Street, Liverpool L3 3AF, United Kingdom

ARTICLE INFO

Article history:
Received 20 May 2022
Received in revised form
25 June 2022
Accepted 25 June 2022
Available online 30 June 2022

Keywords:
Selective laser melting
Ti–6Al–4V
Roughness
surface treatment
Bone-like apatite

ABSTRACT

Medical grade Ti–6Al–4V implants fabricated using selective laser melting (SLM) are recognized as a commercial biomaterial used for bone repairs and fracture fixation. However, there have been cases of failed bone remodeling and implant infections caused by deficient osteointegration. To improve osteogenesis, the Ti implants are treated by acid-etching. This study focused on the effect of surface treatment by using different percentages of sulfuric acid (H_2SO_4), hydrochloric acid (HCL), and hydrofluoric acid (HF) on the SLM Ti–6Al–4V. The microstructure and surface topography before and after treatment were evaluated. Then, the presence of a thicker anatase layer that was detectable on the surface was also observed by X-ray diffraction (XRD). The apatite-forming capabilities which indicated a sample bioactivity were assessed in simulated body fluid (SBF) for periods of 3 days and 7 days. The apatite formed on the surface of sample and XRD scanning revealed the deposition of Ca/P, suggesting successful bone-like apatite. The study discovered that these surface improvements were appropriate for the SLM Ti–6Al–4V prior to clinical applications and were likely to yield higher levels of osseointegration.
© 2022 The Author(s). Published by Elsevier B.V. This is an open access article under the CC BY-NC-ND license (http://creativecommons.org/licenses/by-nc-nd/4.0/).

* Corresponding author.
E-mail address: mzaki.kl@utm.my (M.Z. Hassan).
https://doi.org/10.1016/j.jmrt.2022.06.135
2238-7854/© 2022 The Author(s). Published by Elsevier B.V. This is an open access article under the CC BY-NC-ND license (http://creativecommons.org/licenses/by-nc-nd/4.0/).

1. Introduction

Titanium (Ti) alloy is one of the most commonly used orthopedic implant materials in clinical applications [1]. Among those, Ti–6Al4V is widely utilized in additive manufacturing (AM) as a bioinert substance that can improve osseointegration and enhance the bone-implant contact in open reduction internal fixation (ORIF). Additive manufacturing, specifically selective laser melting (SLM), is a powder bed process that enables irregular and complex-shaped fabrication with high accuracy [2,3]. Therefore, it offers the potential to produce materials that are more precisely suited to anatomical fracture sites than commercially available implants [4]. However, SLM showed surface roughness in the range of 5–20 μm, which may negatively influence tissue regeneration and osseointegration of medical implants that prefer a surface roughness of 3–5 μm for bone remodeling [4,5].

As a result of the poor surface roughness, complications arising from failed bone remodeling after fracture treatment may occur. Bacteria such as *Staphylococcus aureus (S. aureus)*, *Staphylococcus epidermidis*, *Klebsiella pneumoniae*, and *Pseudomonas aeruginosa* colonize the surface of implant and form biofilms [6]. Whereas, for dental implants, *Prevotella intermedia*, *Porphyromonas gingivalis*, and *Fusobacterium nucleatum* are associated with infection [7]. The formation of biofilms further promotes the adherence of multiple species of bacteria on the surface, and thus can lead to chronic infection [8]. These infections are typically due to slow-growing microorganisms such as *Coagulase-negative staphylococci* (CoNS) that commonly live on a person's skin [9]. Bacteria that contribute to the spread and persistence of infections increase the osteoclastic and decrease the osteoblastic activity, causing bone tissue loss known as osteolysis [10]. Infections caused by *S. aureus* can lead to local inflammation implant-associated osteomyelitis such as erythema, swelling, or drainage of pus. Delaying treatment for these infections often results in pseudoarthrosis and soft tissue calcification due to insufficient bone remodeling [11].

Many attempts have been made to improve the surface of titanium alloys, which were hampered by poor cell adhesion and osseointegration [12–15]. Granato et al. [13] stated that the surface of Ti–6Al–4V treated with acid etching (AE) presented a higher mean bone-to-implant contact (BIC) and bone-area-fraction occupancy (BAFO) after 6 weeks in an *in vivo* animal model. This treatment procedure created micro pits on titanium surfaces, which improved osseointegration, and it was suggested that clinical trials be conducted to assess the long-term efficacy of various implant bulk materials. Liang et al. [16] also reported a similar finding, whereby a micro–nanocomposite structure on the titanium surface was obtained after the treatment. After 2 weeks of SBF immersion, apatite formed on the implant surface and thus confirming the bioactivity. Feng et al. [14] seeded rat bone marrow mesenchymal stem cells onto the etched Ti–6Al–4V surface and found that the sample promoted proliferation and differentiation due to its excellent wettability. The cell adhesion increased when the AE time was 5 min, and they noticed that the proliferation increased with increasing AE time. Furthermore, Kim et al. [15] demonstrated that the treated surface SLM Ti–6Al–4V sample exhibited higher hydrophilicity than conventional titanium as a result of roughness enhancement. In addition, Doe et al. [17] inserted the acid-etched implants into rats' long bones and proved no significant toxicity or accumulation of metal ions. This treated Ti–6Al–4V biomaterial was suitable for implantation by offering superior stability and biosafety. Moreover, the substantial improvement of cell attachment on an implant was observed by Sola-Ruiz et al. [18] as a result of the increase of alkaline phosphatase (ALP) and osteocalcin-positive cells following the acid etching.

Surface roughness plays an important role in influencing the cell proliferation and differentiation of SLM Ti–6Al–4V implants. Frequently, modifying this implant could enhance the surface morphology and improve biocompatibility of implant prior to implantation. For example, Jamshidi et al. [19] etched an SLM Ti–6Al–4V sample in Hydrofluoric acid (HF) solution and found the improvement in the cellular affinity and tissue integration. Similarly, Gonzalez et al. [20] demonstrated that acid etching had a greater influence on the surface features of the samples where the osteoblast cells attached to and into the micropores, covering the implant. This osteogenic behavior significantly increases the alkaline phosphatase (ALP) compared to an untreated sample. These micropores can increase osteoblast proliferation, bone-implant contact (BIC) behavior, and bone remodeling, as reported by Xu et al. [21]. Zhang et al. [22] treated the surface of SLM Ti–6Al–4V with a combination of HF and hydrochloric acid (HCL) to evaluate the bioactive response. The treated sample exhibited a super-hydrophilic surface with apatite successfully formed, resulting in excellent biological activity. Tian et al. [23] investigated the effects of AE implant surfaces both *in vitro* and *in vivo*. The findings revealed that a surface with an appropriately sized microgroove/nanopore topography exhibited more satisfactory adhesive and osteogenic efficiency than the conventionally used implant surface in the market. The sample increased the protein expressions of Integrin alpha-2 precursor (ITGA2), phosphatidylinositol 3-kinase (PI3K), and phosphorylated serine/threonine kinase Akt (p-Akt) to enhance osseointegration. The adsorption of proteins onto SLM Ti–6Al–4V was directly related to surface wettability, which was greatly influenced by the surface roughness, as demonstrated by Chen et al. [24]. Soro et al. [25] stated that during SLM, defects were formed that might negatively affect the biological performance of an implant. Therefore, undergoing post-treatment is crucial. After AE, adequate penetration of etchant into the sample was found, thereby reducing the surface defects. Despite the many studies of improving the surface roughness via AE technique, only a limited number of studies have been reported to evaluate the effect of the combination of HF, HCL, and H_2SO_4 on the biological performance of SLM Ti–6Al–4V.

This study aimed to investigate the effect of surface treatment of SLM Ti–6Al–4V. Initially, the SLM Ti–6Al–4V alloy was subjected to acid etching (AE) to improve the surface morphology and roughness. The samples were then characterized via surface profiler, scanning electron microscopy (SEM), and X-Ray Diffraction (XRD). Then, the apatite-forming ability was carried out *in vitro* in SBF to demonstrate the influence of surface treatments on the bioactive performance prior to clinical application.

2. Materials and methods

2.1. Material

The Ti–6Al–4V powder was supplied by SLM Solution Group AG (ASTM F136), and the chemical composition is illustrated in Table 1. The particle size distribution is shown in Fig. 1 after analysis by using a low-vacuum scanning electron microscope LVSEM (M7800F, JOEL Ltd, Tokyo, Japan) at x200 magnification.

The HF and HCL used to treat the sample were supplied by Orioner Hightech Sdn. Bhd. (Setapak, Kuala Lumpur, Malaysia), while H_2SO_4 was purchased from BT Science Sdn. Bhd., (Cheras, Kuala Lumpur Malaysia).

2.2. Fabrication of Ti–6Al–4V by additive manufacturing

The Ti–6Al–4V samples were manufactured by using an SLM 125^{HL} (Estlandring, Lübeck, Germany) machine with a maximum power of 400W. The AutoFab software was used to convert the CAD file into STL format to fabricate the 3D shape of Ti–6Al–4V. The parameters of the SLM were based on the following equation (1):

$$E = \frac{P}{vht} \tag{1}$$

Where, laser power (P), scanning speed (v), hatching distance (h), layer thickness (t), and energy density (E) are all factors. The fabricated samples had dimensions of 2 mm × 2 mm x 2 mm and the setting parameters are tabulated in Table 2.

2.3. Acid etching of SLM-built Ti–6Al–4V

To produce 50 ml of 90% H_2SO_4 from 98% molarity, a 46 ml volume of H_2SO_4 was taken and 4 ml of distilled water was added slowly until the 50 ml mark on the measuring cylinder was reached. Steps were repeated for each of the concentrations as summarized in Table 3. The SLM Ti–6Al4V samples were first washed with distilled water, dried, and immersed in concentrations of the acid for a time of 30min.

2.4. Simulated body fluid (SBF)

The *in vitro* apatite-forming ability of the channel implants was examined by using a simulated body fluid (SBF) with pH value of 7.40 and an ion concentration, as illustrated in Table 4. The channel implants remained in SBF for 3 days and 7 days at 36.5 °C after which they were removed from the SBF, washed with distilled water, and dried. This SBF was prepared according to Kokubo et al. [26] by using 8.035g NaCl, 0.355g $NaHCO_3$, 0.225g KCl, 0.231g $K_2HPO_4 \cdot 3H_2O$, 0.311g $MgCl_2 \cdot 6H_2O$, 39 ml 1M HCl, 0.292g $CaCl_2$, 0.072g Na_2SO_4 and 6.118g tris dissolved sequentially together in 1 L of solution based on ISO 23317.

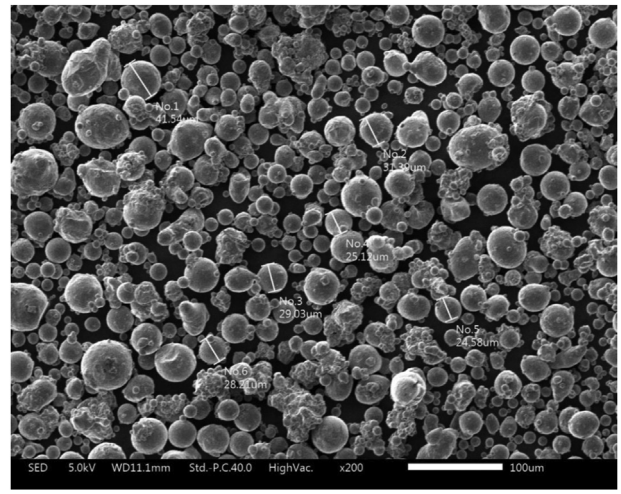

Fig. 1 – The particle size distribution of Ti–6Al–4V.

Table 2 – The input parameters for the fabrication of SLM Ti–6Al–4V.

Parameter	Unit	Value
Laser Power(P)	Watt, W	175
Hatching Distance(h)	mm	0.12
Thickness(t)	µm	30
Scanning Speed(v)	mm/s	697.5

Table 3 – The AE performed in a mixture of H_2SO_4, HCl and HF solution for 30 min.

Sample	H_2SO_4	HCL	HF
Sample A	50%	30%	2%
Sample B	60%	25%	2%
Sample C	70%	20%	2%
Sample D	80%	15%	2%
Sample E	90%	10%	2%
Sample F	Untreated		

2.5. Surface characterization of SLM fabricated Ti–6Al–4V

2.5.1. Density Measurement

The same samples were used for Archimedes. Measurements were performed at room temperature. The mass of the samples was measured before and after AE for each of the samples by using weighing scales (KERN & SOHN GmbH, Balingen, Germany).

Table 1 – Composition of Ti–6Al–4V.

Titanium Alloy	Chemical Composition, %							
	Al	V	Fe	O	H	C	N	Ti
Ti–6Al–4V	5.5	3.5	<0.30	<0.20	<0.0015	<0.08	<0.05	Other

Table 4 – Ion Concentration of Blood Plasma compared to SBF [26].

Ions	Ion Concentration (mM)	
	Blood Plasma	SBF
Na^+	142.0	142.0
K^+	5.0	5.0
Mg^{2+}	1.5	1.5
Ca^{2+}	2.5	2.5
Cl^-	103.0	103.0
HCO_3^-	27.0	27.0
HPO_4^{2-}	1.0	1.0
SO_4^{2-}	0.5	0.5
pH value	7.2–7.4	7.40

2.5.2. SEM

The surface characterizations of the SLM Ti–6Al–4V after AE and SBF immersion had been performed involved field emission scanning (FESEM) (M7800F, JOEL Ltd, Tokyo, Japan).

2.5.3. XRD

The crystallographic structures of the sample were investigated by utilizing X-ray diffractometry (Siemens D5000 Aubrey, Texas, USA) by using Cu Kα radiation (λ = 0.1542 nm) with 40 kV and 40 mA, a step size of 0.05°, a counting time of 80s/step, and a diffraction angle 2Theta between 20° and 90°.

2.5.4. Surface roughness

The surface roughness of the top view of the SLM samples was determined by using an Olympus LEXT 3D Measuring Laser Microscope (OLS4000, Shinjuku, Tokyo, Japan). The main source of light in the Olympus LEXT 3D (OLS4000) was a laser diode emitting a light beam from the visible spectrum with a wavelength, λ = 405 nm.

3. Results and discussion

3.1. Microstructure of untreated SLM Ti–6Al–4V alloy

Figure 2 shows the surface morphology of the untreated SLM Ti–6Al–4V fabricated at a layer thickness of 30 mm and a hatching distance of 0.12 mm, with a laser scanning velocity of 697.5 mm/s. As can be seen in Fig. 2(a), fine needles existed on the uppermost surface attributed to the extremely high cooling rates of the SLM process. These are known as an α′-martensite microstructure, which are aligned at ±45° from the build-up direction and act to restrict the deformation. As a result, the SLM sample could offer significantly higher yield

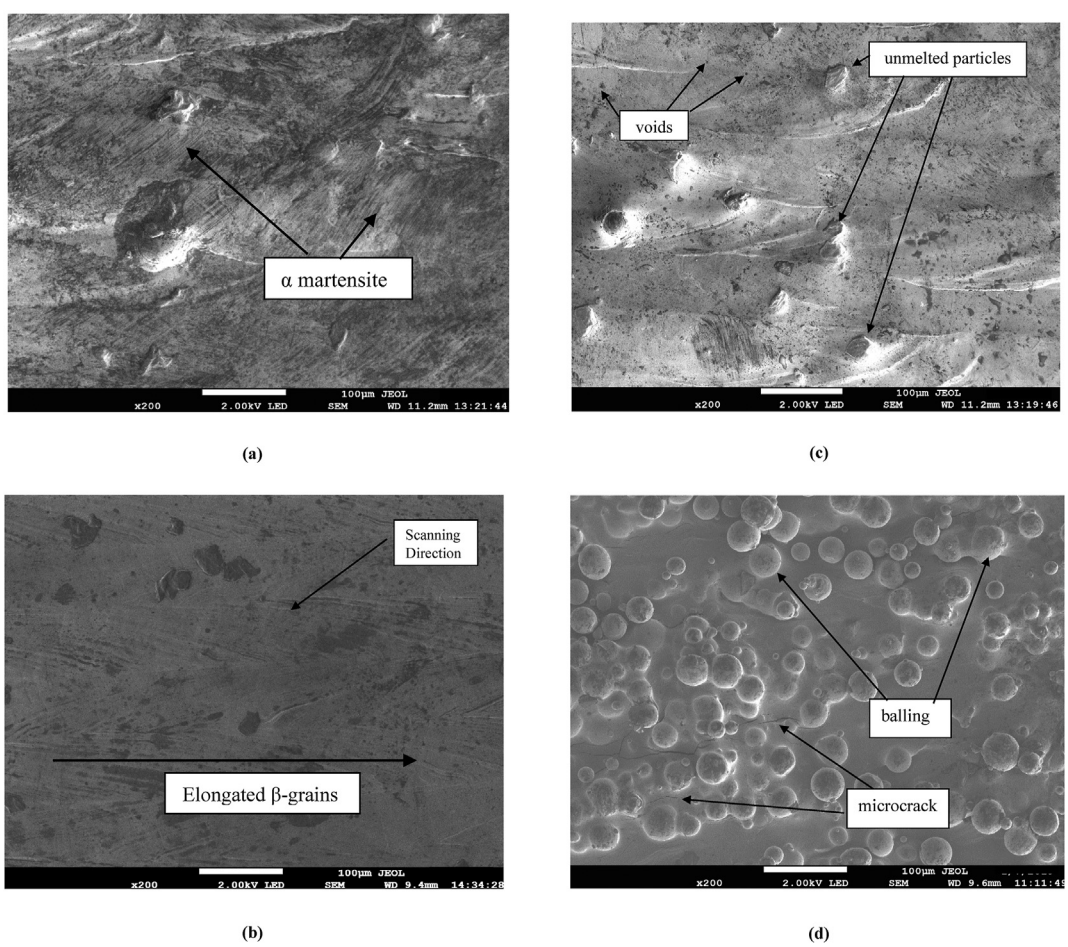

Fig. 2 – Typical micrograph of (a) uppermost surface, (b) β-grains, (c) un-melted particles, and (d) side of untreated SLM Ti–6Al–4V.

strength and ultimate stress. The precipitation of the α′ may lead to the diffusion of the excess vanadium from the supersaturated α' [27,28], which α′ colony size provided excellent mechanical characteristics and ductile fracture mode in SLM Ti–6Al–4V failure. However, the presence of undesired α martensite caused inadequate ductility in columnar prior-β grains because of their low capacity to tolerate crack initiation and propagation [29,30]. The crack propagations on the uppermost sample were clearly obtained on the SLM samples as shown in Fig. 2(a). These defects were commonly caused by the unstable melt-pools due to the non-optimum process parameters in SLM processing [31].

Figure 2(b) illustrates the untreated surface of SLM Ti–6Al–4V toward the scanning direction. This uppermost view reveals long, columnar grains which are oriented in the building direction. These were identified as prior-β grains which were up to several millimeters in length and grew epitaxially during the scanning process as a result of large temperature gradients in the region induced by repeated re-melting and re-heating. The grains were very reliant on heat conduction, and they moved in the same direction as the scanning direction. Therefore, the formation of β-Ti could be caused by lower heat conduction during the melting of the powder playing a significant role in determining the orientation of the grains. These β-Ti precipitates arose from the decomposition of α' martensite during the annealing process. The scanning pattern, local heat transfer, and temperature gradient could all influence the preceding grain boundaries [32,33].

Figure 2(c) demonstrates an untreated SLM surface with a significant proportion of un-melted particles and voids. It happens caused by massive temperature differences in the heat transfer between the powder and solidification of melt pool during fabrication. The SLM Ti–6Al–4V process involves fine metal powders that are melted by a laser beam moving at a very high speed. Therefore, this melting process may create external defects, resulting in some of the powder being blown off. Due to this inherent issue, as-fabricated parts usually have partially melted particles on the surface when the given energy density is inadequate to totally melt the powder. The un-melted powder remained on the layer and caused porosity. This complete coverage of un-melted particles formed on the surface may be attributed to the higher surface roughness of the untreated SLM Ti–6Al–4V [34,35]. In addition, pores (Fig. 2(c)) occurred due to the high cooling rate during the solidification process, which dissolved gas was trapped in the molten pool. When high laser energy was applied to the molten pool, pores were created by gas bubbles confined between the layers [36]. According to Williams et al. [37], larger melt pools of SLM Ti–6Al–4V created greater voids, which might lead to fracture initiation on the surface and lower fatigue life.

Figure 2(d) represents the balling and micro-cracking that exist on the side surface of SLM Ti–6Al–4V. Balling is generally associated with the formation of several metallic agglomerates as spherical or ellipsoidal balls caused by the powder particles adhering to the SLM sample surface. During the layer-by-layer process, the balling phenomenon occurs due to the low level of liquid aggregation with the solid particle, which eventually retards the liquid flow and particle rearrangement, leading to the formation of different-sized balls on the sample surface. The low energy input and low laser power followed by the high scanning speed cause the formation of balling due to insufficient melting and wetting with the surrounding parts [38]. These phenomena eventually lead to higher surface roughness of the SLM Ti–6Al–4V sample and greatly affect the fatigue performance of the SLM Ti–6Al–4V. The micro-cracks (Fig. 2(d)) initiated by the partially melted particles were caused by the shrinkage rate between the solidifying melt and the powder particles. As a result, micro-cracks occurred between the melt pool and the partially molten powder particles. The micro-cracks formed along the grain boundaries between the α' martensite in the microstructure of the SLM Ti–6Al–4V, which eventually reduced the ductility of an SLM-fabricated sample [39].

3.2. *Acid etching of SLM Ti–6Al–4V*

In general, AE treatment is used to modify the SLM Ti–6Al–4V surface, which may help lessen the effects of hydrogen generation on titanium embrittlement. Figure 3 summarizes the effect on sample density after AE treatment. As can be seen, after AE treatment for 30 min, the average mass loss ranged from 10% to 30%, and was associated with the removal of unmelted particles. The reduction in mass was more pronounced when a higher acid concentration was used. It was also related to immersion time and was attributed to factors such as surface passivation. The highest weight loss was observed for Sample E, which may be caused by the penetration of H_2SO_4 and HF into the samples due to improved permeability. At a high concentration, the hydrogen generation was negligible, so the structural wettability and absorption exerted the most influence. The decreased sample mass with increasing treatment time resulted in effectively removing the partially sintered powder particles attached to the surface. According to Bezuidenhout et al. [40], after 30 min of AE immersion, the sample mass decreased, and brown nitrogen dioxide (NO2) gas was emitted. The combined reaction is proposed in Equation (2).

$$\mathrm{Ti} + 6\mathrm{HF} + 2\mathrm{HNO_3} \rightarrow [\mathrm{TiF_6}]^{2-}\ \mathrm{NO_2} + \mathrm{NO} + 2\mathrm{H} + 3\mathrm{H_2O} \tag{2}$$

Figure 4 shows the SEM images of Sample A, Sample B, Sample C, Sample D, and Sample E following AE treatment. Overall, this process effectively removes the partly melted and retained metal particles from the surface of the samples. Figure 4 (a) illustrates a rougher layer, protuberances, and a submicron-nanoporous morphology texture, which could be related to the formation of an oxide film and irregular coarseness that form on the outer surface. This specific morphology positively affects the osseointegration of implantable devices to promote the adhesion of fibrin and osteogenic cells. In addition, a protuberance and spheroid-like shape were observed in Sample B (Fig. 4(b)). It was owing to the adoption of the balling effect that was introduced during the initial fabrication process. In contrast, the presence of micropores and protrusions were obtained in Sample C ((Fig. 4(c)) and Sample D (Fig. 4(d)). These micropores were formed because of surface imperfections. A combination of pit and

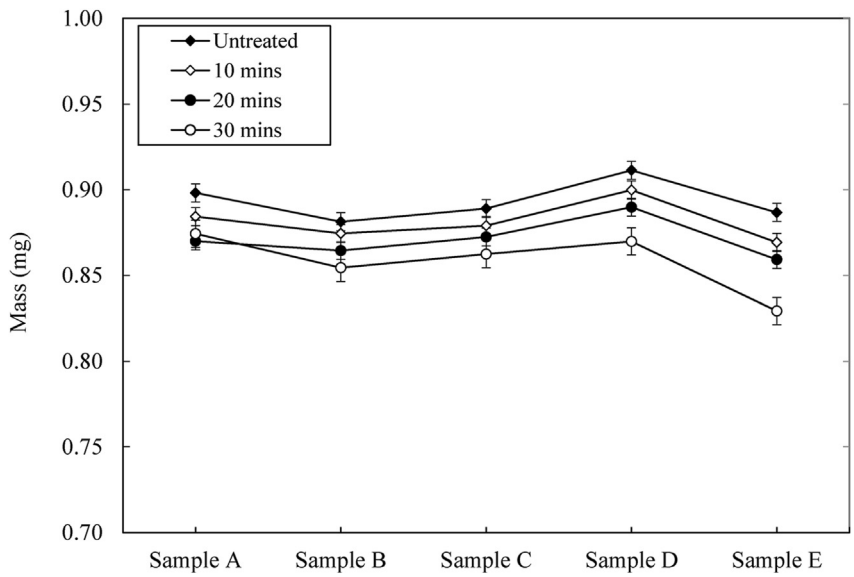

Fig. 3 – Typical mass of SLM Ti–6Al–4V measured following AE treatment.

valley surfaces significantly increases the proliferation and cell viability in biomedical implants. A rougher topographical feature allows protein attachment and improves the bone-implant contact after implantation [41]. Some microcracks were also observed on Sample D, due to corrosive behavior of H_2SO_4. On the other hand, Sample D shows fewer protrusions with several spots of smooth surface as compared to Sample C. Nonetheless, Sample E (Fig. 4(e)) was significantly smoother after the acid etching treatment. It can be suggested that an increasing concentration of H_2SO_4 resulted in a finer sample surface and removed most of the residual. Some cracks were also noticed due to TiO_2 layer deterioration, mainly originating from the oxidization of the α-phase. Then, the SO_4^{2-} ions that exist on the surface, form a passive film and penetrate the crack. This α-structure might easily dissolve, creating pits and subsequently leading to the expansion of the corrosion area [42].

3.3. *Roughness and morphology of acid etched samples*

Figure 5 depicts a roughness profile for each of the samples after the AE process. In general, for all the treatments investigated in this study, specimens had a nearly identical surface roughened. In general, the average roughness (Ra) value for the five distinct Ti–6Al–4V specimens was between 1.56 μm and 2.52 μm. However, the maximum Rz value ranged between 12.71 μm and 19.30 μm. It was attributed to pit-valley creation and the formation of an oxide layer on the sample surfaces [43].

Besides the Ra, Rq, and Rz surface height parameters, it is possible to further characterize the surface roughness by performing a statistical analysis on the roughness data. The skewness (Rsk) and the kurtosis (Rku) are relevant surface roughness parameters that allow a deeper understanding of surface morphology. Figure 6 shows the (Rsk) and the (Rku) mean values for the roughness profiles of the different Ti–6Al–4V specimens. Based on Fig. 6, it was clear that Samples B, D and E showed Rsk to be negative, which indicated that the AE surface led to a particular topography which deep valleys are predominant in the sample. The sharp peaks formed are effective for load-bearing applications which correlate with this work. The kurtosis (Rku) parameter showed that all the tested specimens (Sample A to Sample E) presented a flat height distribution (Rku <4). These two roughness parameters allowed a more comprehensive understanding of the influence of the topography on the tribological behavior and osseointegration of these Ti–6Al–4V surfaces by indicating the low number of high peaks and predominance of deep valleys.

Nevertheless, Sample C yields the highest Ra, which indicates the beta phase ratio in the samples. It should also be noted that the $\beta > \alpha > \alpha'$ phase structures cause the resistance in the etched surface, with increases in the β phase causing decreased Ra values. Previous studies show that Ra values of 1 μm–5 μm can promote cell proliferation and osseointegration for biomedical implants [44–46]. In this study, the maximum height of the Rz profile was obtained between 12.7 and 19.3 μm. This high surface roughness can be said to be due to the thickness of the oxide layer formed that is generated by the 20% HCl [47]. HCl is a nonoxidizing acid, titanium is only modestly resistive to ferric chloride solutions. However, the Ra value for Sample E increased significantly due to the larger volumes of debris and the number of fractures generated by the corrosive action of 90% H_2SO_4.The Ra parameter of samples produced decreased after AE with HF as this treatment completely removed the oxides formed during raw powder processing. High roughness can limit cell growth space, forcing deposited cells into their sedimentation stage [48]. The poor surface finish obtained during SLM was caused by the presence of partially unmelted particles and the balling phenomenon, as illustrated in Fig. 2. This caused limited space for cells to adhere, leading to low initial attachment and subsequent proliferation which resulted in the poor biological behavior exhibited by the as-built sample [49].

The native SLM sample yielded an Ra of 5 μm–20 μm. This native SLM Ti–6Al–4V showed that the higher surface

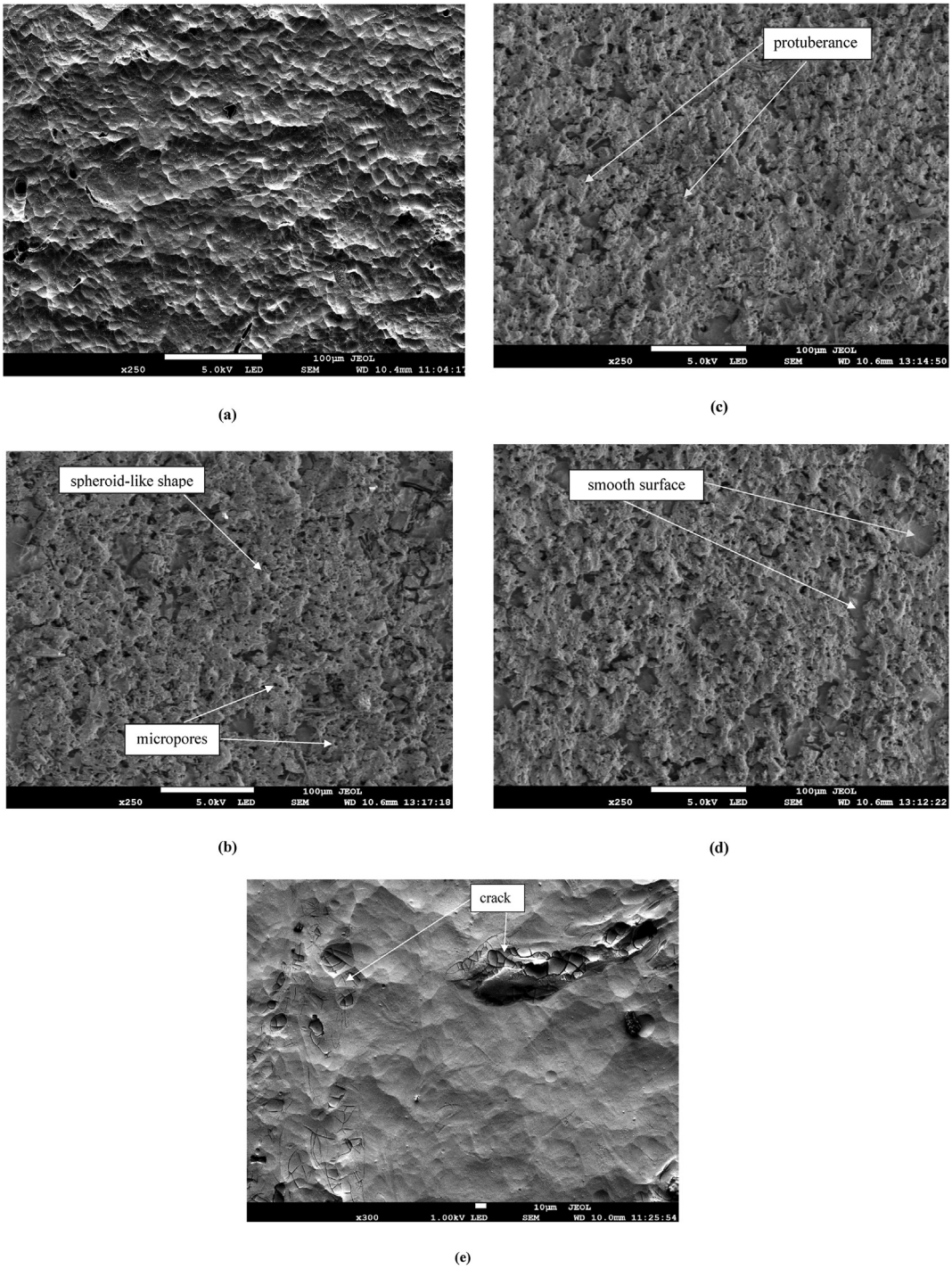

Fig. 4 – Typical SEM images of (a) Sample A, (b) Sample B, (c) Sample C, (d) Sample D and (e) Sample E SLM Ti–6Al–4V after AE treatment.

roughness caused by the processing parameter could lead to multiple stress concentrations, which eventually caused crack initiation on the SLM surface [50]. In addition, the corresponding surface roughness of the SLM sample showed Ra increased as the percentage of H_2SO_4 increased. The increase in roughness was mainly caused by mixtures with high percentages of H_2SO_4/HCl and the subsequent increase in the surface roughness of SLM-Ti by producing a micrometer-scale roughness condition. The acid etched samples caused hydrogen desorption to occur, which consequently led to the presence of a titanium hydride (TiH_2) on the surface, leading to the increased roughness of SLM-produced samples [51].

3.4. *Apatite-forming ability of SLM Ti–6Al–4V in SBF*

Specifically, the bioactivity of fabricated SLM Ti–6Al–4V was investigated by determining the apatite layer on the surface of the samples. Samples were then submerged in the SBF

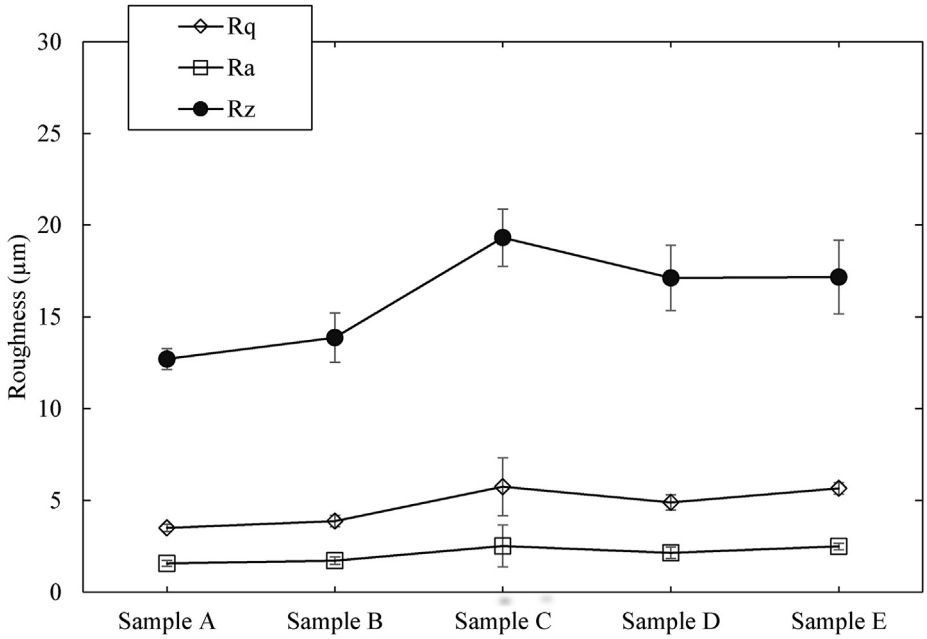

Fig. 5 – Ra, Rq, and Rz surface roughness parameters of SLM Ti–6Al–4V top surface.

solution after being pretreated with the AE procedure. Generally, the surface of all specimens was homogeneously covered by a layer of Ca/P after 3 days of immersion. This Ca/P layer consisted of apatite that formed as a byproduct of SBF immersion. When the treated Ti alloy was immersed in SBF, the Ca^{2+} ions released, and the pH value of the surrounding fluid increased. It is intended to enhance ionic activity and generate Ti–OH groups on SLM samples as shown in Fig. 7. As Ca^{2+} ions accumulate, the Ti surface becomes positive ions and interacts with negatively charged phosphate ions to generate amorphous calcium phosphate. This calcium phosphate is ultimately converted into bone-like crystalline apatite.

Figure 8 illustrates the morphological transformation for Sample A, Sample B, Sample C, Sample D, and Sample E of SLM Ti–6Al–4V after 3 days of immersion in SBF. As seen in Sample A (Fig. 8(a)), globules apatite mostly covered the outer surfaces. In contrast, the area of Sample B (Fig. 8(b)) was dominated by crystals and precipitates. The precipitate that developed on both surfaces was Ca/P derived from calcium phosphate. Samples A and B clearly had smaller crystals, while Samples C (Fig. 8(c)), Sample D (Fig. 8(d)), and Sample E (Fig. 8(e)) had larger clusters and more precipitates. In addition, microcracks were seen on the Sample D surfaces. An obvious crack was also obtained from Sample E. It can be suggested that increasing H_2SO_4 concentration lengthens the crack on the Ti-alloy surface and tends to lead to corrosion. Nevertheless, this Ti-alloy also exhibited low corrosion resistance due to the presence of α' phases. Shi et al. [52] reported that the corrosion rate of an SLM Ti–6Al–4V submerged in H_2SO_4 was greater than that of other acid solutions. Also, Samples D and Sample E showed relatively small spheroidal structures in the form of elongated aggregates produced on the surface of the samples. This chemical treatment homogenously improves the micro/nanostructures on the surface of an implant [53,54] and is beneficial for bone-like apatite formation [55].

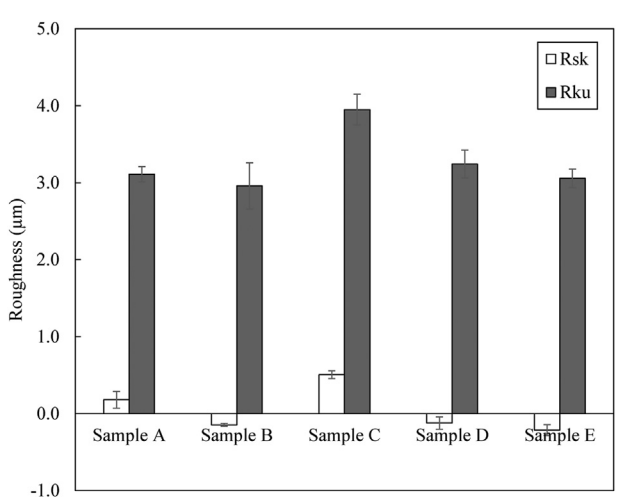

Fig. 6 – Surface roughness of Rsk and Rku of SLM Ti–6Al–4V.

The apatite-forming activity was further evaluated by the immersion in SBF for 7 days. The results showed a drastic improvement in apatite formation, as illustrated in Fig. 9(a). Figure 9(b) thereby confirmed that the bioactivity occurred which a compact and homogeneous apatite layer was observed as a layer of Ca/P deposit. The Ca/P formation for sample C in Fig. 9(c) was higher than after 3 days immersion in SBF. Whereby, XRD indicated that uniform elongated apatite crystals formed which suggested that the Ra of 2.50 μm favored the formation of Ca/P. As for Fig. 9(d), there were uniform apatite formed on the surface. However, the presence of cracks, which may be attributed to the higher percentage of H_2SO_4 produced pits or microcracks. Nevertheless, similar

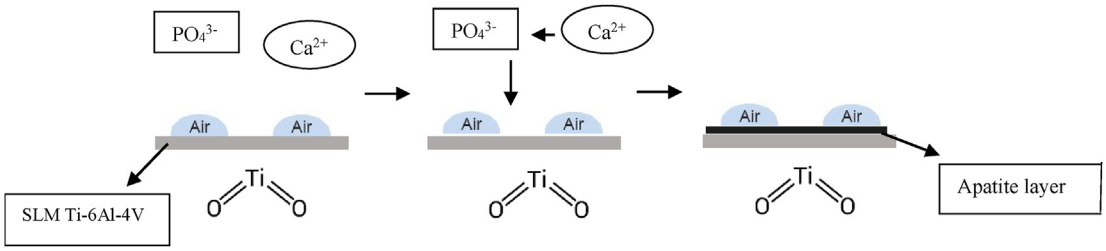

Fig. 7 – Schematic drawing of the mechanism of apatite formation on the SLM Ti–6Al–4V.

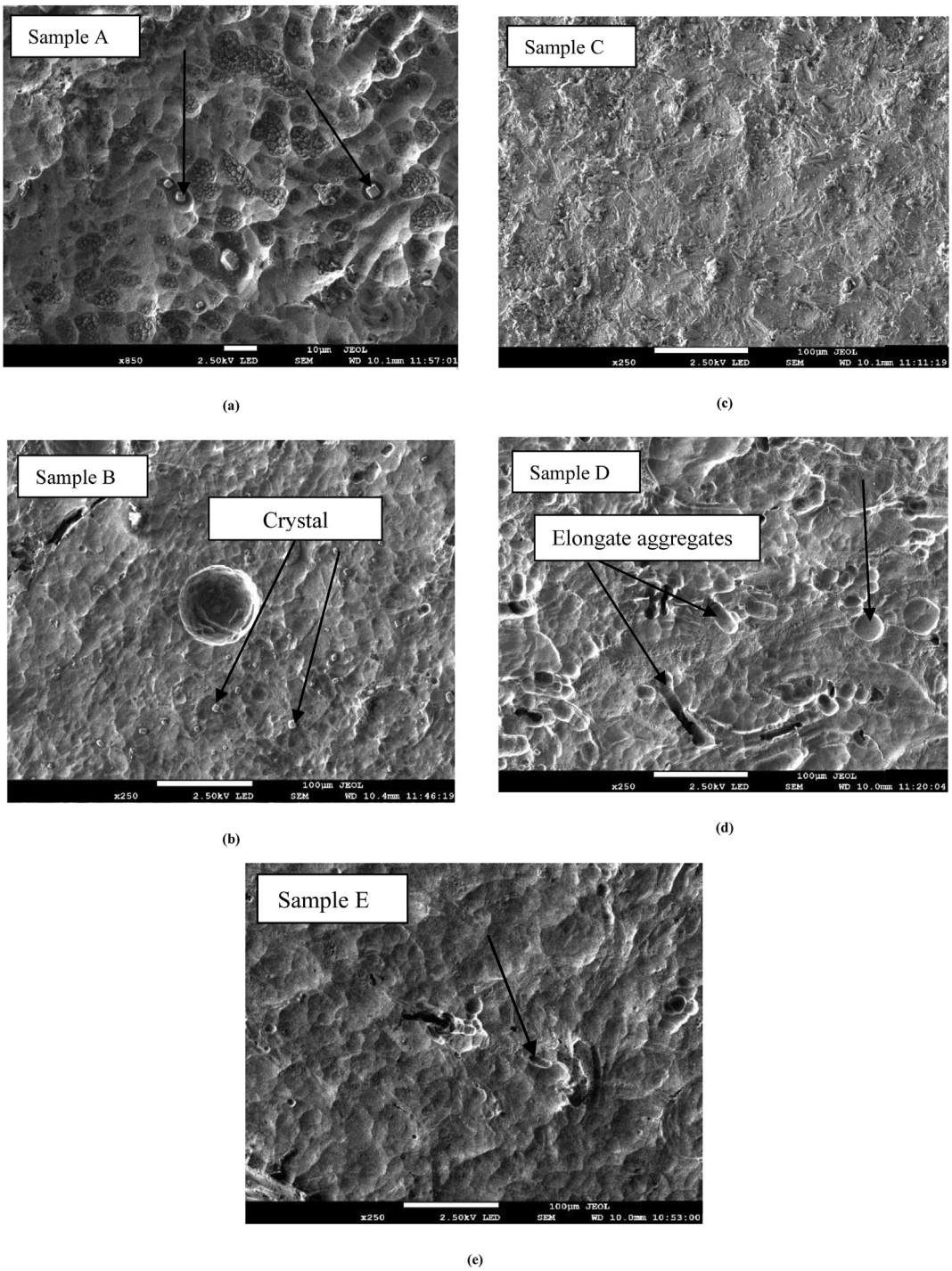

Fig. 8 – Morphological changes for (a) Sample A, (b) Sample B, (c) Sample C, (d) Sample D and (e) Sample E of SLM Ti–6Al–4V after 3 days immersed in SBF.

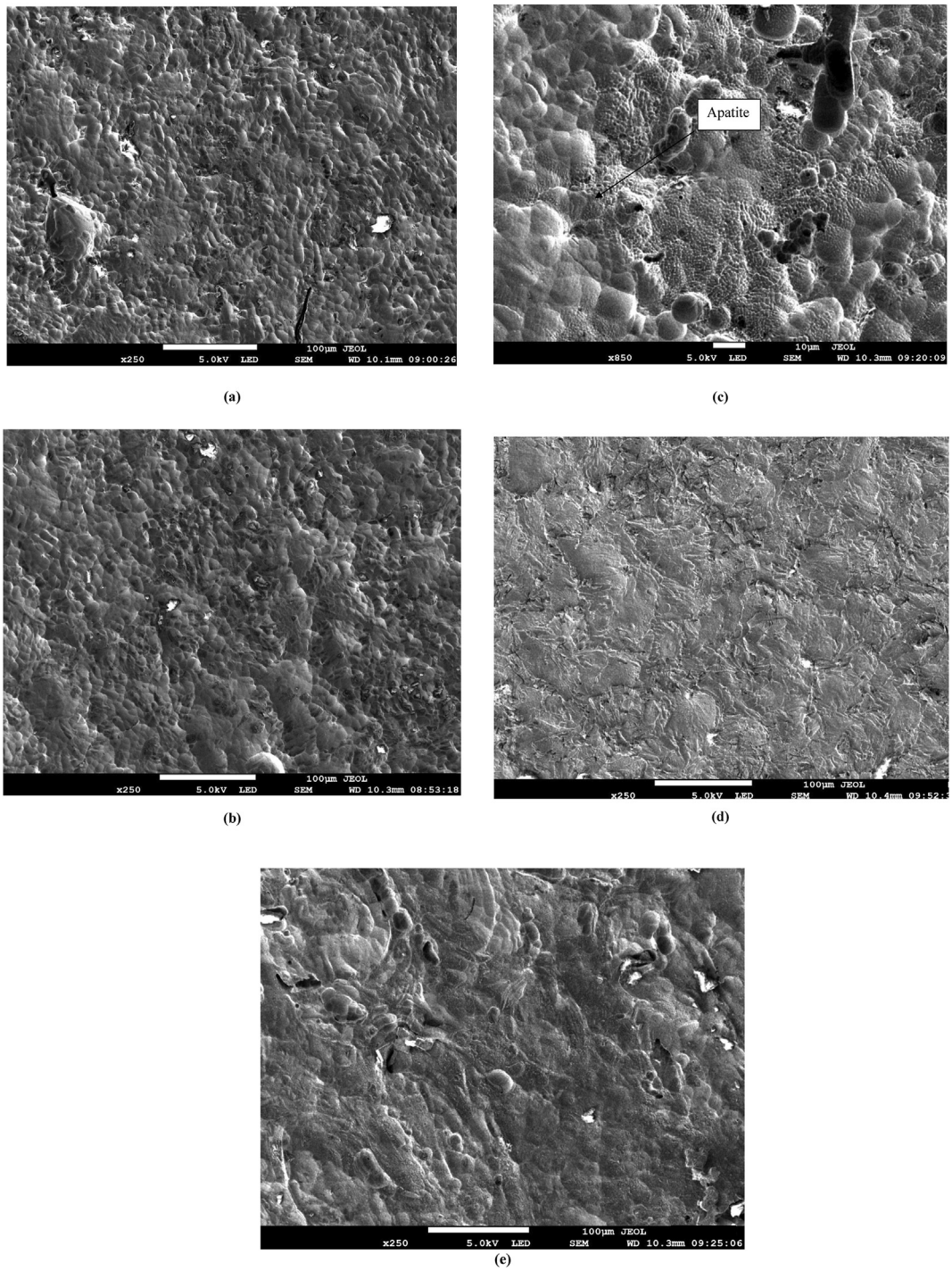

Fig. 9 – Morphological changes of (a) Sample A, (b) Sample B, (c) Sample C, (d) Sample D and (e) Sample E SLM Ti–6Al–4V after 7 days immersed in SBF.

cracks formed on Sample E in Fig. 9(e) after 7 days of SBF. The formation of cracks might be from the SBF that penetrated the porous layer and reacted with the inner compact layer from the corrosive behavior of strong acids from the AE treatment. The corrosive behavior of SBF and found that SLM Ti–6Al–4V showed the lowest corrosion potential as compared to other AM methods such as EBM [56]. This indicated that SLM is more favorable for biomedical applications as compared to other AM methods.

3.5. *XRD Crystallinity*

XRD analysis was performed on the SLM Ti–6Al–4V samples to assess the influence of treatment and SBF immersion on the crystalline structure of the samples. Figure 10 presents the XRD spectra of Sample B, Sample D and Sample E following SBF immersion for 7 days. From the XRD pattern, α and α' martensite is characterized by their similar structure. However, the presence of a rutile TiO2 phase in the XRD diffraction peaks

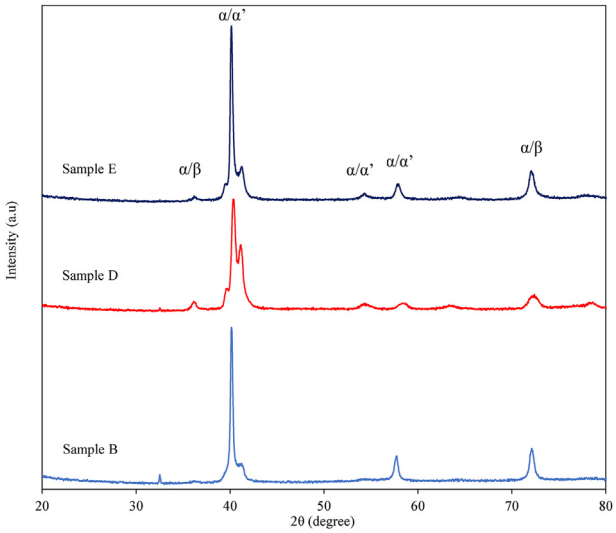

Fig. 10 – XRD diffraction pattern of α, α′, and α/β of SLM Ti–6Al– 4V following immersion in SBF for 7 days.

(38°- 43°) for all the samples is attributed to higher heat during the SLM process [57]. Therefore, it was difficult to distinguish between the α and α' phases because they had the same crystal structure and similar lattice parameters. From the figure, XRD peaks were clearly visible in Sample A and Sample D, and the low intensity of these peaks in Sample E was related to the small thickness of the oxide layer. Sample D shows an intensity increase at the peaks, indicating the thickening of the apatite layers after soaking in SBF for 7 days. The low-intensity XRD peaks also observed in Sample D were assigned to anatase TiO_2 (2 Theta = 32.52° and 85.40°). The anatase layer thickness was estimated to be about 25 nm–50 nm [58]. On the other hand, the TiO_2 stimulated the apatite structure after the SBF immersion in AM Ti–6Al–4V. The SLM process was characterized by a fast-cooling rate, which will influence the microstructure of Ti–6Al–4V by increasing the needle-shaped β phase which was significant in Sample B. The SLM fast cooling rate promoted a transformation from β phase to the martensitic α′ phase. As for the β phase, it was more favorable than the α phase for assisting nucleation and growth of the apatite structure on the surface due to their different crystal structures. During the AE, the passive film coating of SLM Ti–6Al–4V was completely dissolved [as based on equation (3)], which suggested that the present oxide layer was thinner as compared to the untreated sample [59–61]. After soaking in SBF for 7 days, the ions from the titanate layer exchanged with the H_3O^{3+} leading to the formation of Ti–OH groups on the surface of the treated sample. This influenced the ability for apatite formation due to the presence of the rutile oxide phase (TiO_2) and increased the corrosion resistance of the SLM Ti–6Al–4V which prevents the release of ions into the body fluid [62]. The XRD pattern of the untreated sample did not reveal the formation of any oxide phase on its surface since no characteristic peaks of oxide phases were observed. The TiOH is incorporated with the Ca^{2+}, the byproduct of SBF, to provide the nuclei for apatite formation. These negatively charged PO_4^{3-} ions form a Ca–P layer which crystallized into bone-like apatite as suggested by the following equation (4).

$$TiO_2 + 4HCl \rightarrow TiCl_4 + 2H_2O \quad (3)$$

$$10Ca^{2+} + 6PO_4^{3-} + 2OH \rightarrow Ca_{10}(PO_4)\,6(OH)_2 \quad (4)$$

4. Conclusion

In this study, the SLM Ti–6Al–4V was treated by using acid etchings at different percentage concentrations. The amount of apatite formed for each sample was then determined by immersing them in SBF. The main findings of this research are:

1. The as-built Ti–6Al–4V showed an out-of-equilibrium microstructure with very fine α′ martensitic laths, unmelted particles, and crystallographic defects. After the AE process, there was improvement in the surface of the SLM Ti–6Al–4V with fewer crystallographic defects. Also, β grain boundaries were not observed.
2. A higher surface roughness resultant from balling, voids, staircase-chapping, and unmelted particles is mostly due to layer-by-layer fabrication of Ti–6Al–4V parts. The AE reduced the defects and then formed a uniform and relatively smooth titanium surface. Still, treating the samples with a high concentration of H_2SO_4 makes the samples corrode more quickly. This causes pits and cracks to form, which reduces the formation of bone-like apatite in SBF.
3. After the samples were treated by acid etching, the presence of a thicker anatase layer and the formation of a stable titanium oxide layer were detectable by X-ray diffraction, indicating good bioactivity.
4. After soaking in SBF, thick apatite layers consisting of Ca/P formed on the surface. The amount of apatite formed increased continuously under the SEM observation with the duration of time soaking

Declaration of Competing Interest

The authors declare that they have no known competing financial interests or personal relationships that could have appeared to influence the work reported in this paper.

Acknowledgment

This study was supported financially by UTMSPACE - School of Professional and Continuing Education with Quick Win Research Grant Scheme R.K130000.7756.4J573 and Universiti Sains Islam Malaysia with 'Geran Universiti 2022′ initiative PPPI/FPSK/0122/USIM/14002.

REFERENCES

[1] Zhang LC, Chen LY. A review on biomedical titanium alloys: Recent Progress and Prospect. Adv Eng Mater 2019;21:1–29.
[2] Aufa AN, Hassan MZ, Ismail Z. Recent Advances in Ti-6Al-4V additively manufactured by selective laser melting for

biomedical implants: Prospect Development. J Alloys Compd 2021;896:163072.
[3] Yu X, Xu R, Zhang Z, Jiang Q, Liu Y, Yu X, et al. Different cell and tissue behavior of micro-/nano-Tubes and micro-/nano-Nets Topographies on selective laser melting titanium to enhance osseointegration. Int J Nanomedicine 2021;16:3329–42.
[4] Ginestra P, Ferraro RM, Zohar-Hauber K, Abeni A, Giliani S, Ceretti E. Selective laser melting and electron beam melting of Ti6Al4V for orthopedic applications: a Comparative study on the applied building direction. Mater 2020;13.
[5] Aufa AN, Hassan MZ, Ismail Z. The fabrication of titanium alloy biomedical implants using additive manufacturing: a Way Forward. J. Met. Mater. Miner. 2021;7:39–48.
[6] Gao Q, Feng T, Huang D, Liu P, Lin P, Wu Y, et al. Antibacterial and hydroxyapatite-forming coating for biomedical implants based on polypeptide-functionalized titania nanospikes. Biomater Sci 2019;8:278–89.
[7] Rumbaugh KP, Sauer K. Biofilm dispersion. Nat Rev Microbiol 2020;18:571–86.
[8] Souza JCM, Sordi MB, Kanazawa M, Ravindran S, Henriques B, Silva FS, et al. Nano-scale modification of titanium implant surfaces to enhance osseointegration. Acta Biomater 2019;94:112–31.
[9] Noremylia MB, Hassan MZ, Ismail Z. Recent advancement in isolation, processing, characterization and applications of emerging nanocellulose: a review. Int J Biol Macromol 2022;206:954–76.
[10] Chouirfa H, Bouloussa H, Migonney V, Falentin-Daudré C. Review of titanium surface modification techniques and coatings for antibacterial applications. Acta Biomater 2019;83:37–54.
[11] Aufa AN, Hassan MZ, Ismail Z. Recent Progress of Sol-gel coating of pure Magnesium in biomedical applications. A review. Malaysian Journal of Medicine and Health Sciences 2021;17.
[12] Philip JT, Mathew J, Kuriachen B. Tribology of Ti6Al4V: a review. Friction 2019;7:497–536.
[13] Granato R, Bonfante EA, Castellano A, Khan R, Jimbo R, Marin C, et al. Osteointegrative and microgeometric comparison between micro-blasted and alumina blasting/acid etching on grade II and V titanium alloys (Ti-6Al-4V). J Mech Behav Biomed Mater 2019;97:288–95.
[14] Feng F, Wu Y, Xin H, Chen X, Guo Y, Qin D, et al. Surface characteristics and biocompatibility of Ultrafine-grain Ti after Sandblasting and acid etching for dental implants. ACS Biomater Sci Eng 2019;5:5107–15.
[15] Kim J, Lee H, Jang T-S, Kim D, Yoon C-B, Han G, et al. Characterization of titanium surface modification Strategies for osseointegration enhancement. Metals 2021;11:618.
[16] Liang C-Y, Jiang X-J, Ji R-L, Li B-E, Zou X-R, Wang H-S, et al. Preparation and surface modification of 3D printed Ti–6Al–4V porous implant. Rare Met 2020;40:1164–72.
[17] Doe Y, Ida H, Seiryu M, Deguchi T, Takeshita N, Sasaki S, et al. Titanium surface treatment by calcium modification with acid-etching promotes osteogenic activity and stability of dental implants. Materialia 2020;12. 100801-100801.
[18] Sola-Ruiz MF, Perez-Martinez C, Labaig-Rueda C, Carda C, Martín De Llano JJ. Behavior of Human osteoblast cells cultured on titanium Discs in relation to surface roughness and presence of Melatonin. Int J Mol Sci 2017;18:823. 823.
[19] Jamshidi P, Aristizabal M, Kong W, Villapun V, Cox SC, Grover LM, et al. Selective laser melting of Ti-6Al-4V: the Impact of post-processing on the tensile, fatigue and biological properties for medical implant applications. Mater 2020;13:2813.
[20] González JE, Armas Gd, Negrin J, Beltrán AM, Trueba P, Gotor FJ, et al. Influence of successive chemical and Thermochemical treatments on surface features of Ti6Al4V samples manufactured by SLM. Metals 2021;11:313.
[21] Xu JY, Chen XS, Zhang CY, Liu Y, Wang J, Deng FL. Improved bioactivity of selective laser melting titanium: surface modification with micro-/nano-textured hierarchical topography and bone regeneration performance evaluation. Mater. Sci. Eng. C Mater. Biol. Appl. 2016;68:229–40.
[22] Zhang X, Wan Y, Liu Z, Wang H, Yu M, Liu A, et al. Preparation and bioactive response of super-hydrophilic surface on selective laser melting titanium. Procedia CIRP 2020;89:222–7.
[23] Tian Y, Zheng H, Zheng G, Hu P, Li Y, Lin Y, et al. Hierarchical microgroove/nanopore topography regulated cell adhesion to enhance osseointegration around intraosseous implants in vivo. Biomater Sci 2022;10:560–80.
[24] Chen Z, Yan X, Yin S, Liu L, Liu X, Zhao G, et al. Influence of the pore size and porosity of selective laser melted Ti6Al4V ELI porous scaffold on cell proliferation, osteogenesis and bone ingrowth. Mater Sci Eng, C 2020;106:110289.
[25] Soro N, Saintier N, Attar H, Dargusch MS. Surface and morphological modification of selectively laser melted titanium lattices using a chemical post treatment. Surf Coat Technol 2020;393:125794.
[26] Kokubo T, Yamaguchi S. Simulated body fluid and the novel bioactive materials derived from it. J Biomed Mater Res 2019;107:968–77.
[27] Sallica-Leva E, Caram R, Jardini AL, Fogagnolo JB. Ductility improvement due to martensite alpha' decomposition in porous Ti-6Al-4V parts produced by selective laser melting for orthopedic implants. J Mech Behav Biomed Mater 2016;54:149–58.
[28] Cao S, Chu R, Zhou X, Yang K, Jia Q, Lim CVS, et al. Role of martensite decomposition in tensile properties of selective laser melted Ti-6Al-4V. J Alloys Compd 2018;744:357–63.
[29] Xu W, Lui EW, Pateras A, Qian M, Brandt M. In situ tailoring microstructure in additively manufactured Ti-6Al-4V for superior mechanical performance. Acta Mater 2017;125:390–400.
[30] Valente EH, Jellesen MS, Somers MAJ, Christiansen TL. Gaseous surface hardening of Ti-6Al-4V fabricated by selective laser melting. Surf Coat Technol 2020;383.
[31] Sadali MF, Hassan MZ. Influence of selective laser melting scanning speed parameter on the surface morphology , surface roughness , and micropores for manufactured Ti6Al4V parts. 2020. p. 1–11.
[32] Ali H, Ma L, Ghadbeigi H, Mumtaz K. In-situ residual stress reduction, martensitic decomposition and mechanical properties enhancement through high temperature powder bed pre-heating of Selective Laser Melted Ti6Al4V. Mater. Sci. Eng. A 2017;695:211–20.
[33] Thijs L, Verhaeghe F, Craeghs T, Humbeeck JV, Kruth J-p. A study of the microstructural evolution during selective laser melting of Ti − 6Al − 4V. Acta Mater 2010;58:3303–12.
[34] Chen C, Hao Y, Bai X, Ni J, Chung S-M, Liu F, et al. 3D printed porous Ti6Al4V cage: effects of additive angle on surface properties and biocompatibility; bone ingrowth in Beagle tibia model. Mater Des 2019;175.
[35] Shi X, Ma S, Liu C, Chen C, Wu Q, Chen X, et al. Performance of high layer thickness in selective laser melting of Ti6Al4V. Mater 2016;9:975.
[36] Zhang B, Li Y, Bai Q. Defect formation mechanisms in selective laser melting: a review. Chin J Mech Eng 2017;30:515–27.
[37] Tammas-Williams S, Withers PJ, Todd I, Prangnell PB. The influence of porosity on fatigue crack initiation in additively manufactured titanium Components. Sci Rep 2017;7:7308.
[38] Li R, Liu J, Shi Y, Wang L, Jiang W. Balling behavior of stainless steel and nickel powder during selective laser melting process. Int J Adv Manuf Technol 2012;59:1025–35.

[39] Dareh Baghi A, Nafisi S, Hashemi R, Ebendorff-Heidepriem H, Ghomashchi R. Effective post processing of SLM fabricated Ti-6Al-4 V alloy: Machining vs thermal treatment. J Manuf Process 2021;68:1031–46.
[40] Bezuidenhout M, Ter Haar G, Becker T, Rudolph S, Damm O, Sacks N. The effect of HF-HNO3 chemical polishing on the surface roughness and fatigue life of laser powder bed fusion produced Ti6Al4V. Mater Today Commun 2020;25.
[41] Ran Q, Yang W, Hu Y, Shen X, Yu Y, Xiang Y, et al. Osteogenesis of 3D printed porous Ti6Al4V implants with different pore sizes. J Mech Behav Biomed Mater 2018;84:1–11.
[42] Sui Q, Meng L, Wang S, Li P, Yin X, Wang L. Effect of Nb addition on mechanical properties and corrosion behavior of Ti6Al4V alloy produced by selective laser melting. J Mater Res 2020;35:571–9.
[43] Sadali MF. Effect of hatching distance on surface morphology and surface roughness of the Ti6Al4V for biomedical implant using SLM process. Malaysian Journal of Microscopy 2019;15:72–82.
[44] Le PTM, Shintani SA, Takadama H, Ito M, Kakutani T, Kitagaki H, et al. Bioactivation treatment with mixed acid and heat on titanium implants fabricated by selective laser melting enhances Preosteoblast cell differentiation. Nanomaterials 2021;11.
[45] Pal S, Finšgar M, Bončina T, Lojen G, Brajlih T, Drstvenšek I. Effect of surface powder particles and morphologies on corrosion of Ti-6Al-4 V fabricated with different energy densities in selective laser melting. Mater Des 2021:211.
[46] Hamza HM, Deen KM, Haider W. Microstructural examination and corrosion behavior of selective laser melted and conventionally manufactured Ti6Al4V for dental applications. Mater. Sci. Eng. C Mater. Biol. Appl. 2020;113:110980.
[47] Torres Y, Sarria P, Gotor FJ, Gutiérrez E, Peon E, Beltrán AM, et al. Surface modification of Ti-6Al-4V alloys manufactured by selective laser melting: microstructural and tribo-mechanical characterization. Surf Coat Technol 2018;348:31–40.
[48] Wu C, Chen M, Zheng T, Yang X. Effect of surface roughness on the initial response of MC3T3-E1 cells cultured on polished titanium alloy. Bio Med Mater Eng 2015;26(1):S155–64.
[49] Jamshidi P, Aristizabal M, Kong W, Villapun V, Cox SC, Grover LM, et al. Selective laser melting of Ti-6Al-4V: the Impact of post-processing on the tensile, fatigue and biological properties for medical implant applications. Mater 2020;13.
[50] Liu S, Shin YC. Additive manufacturing of Ti6Al4V alloy: a review. Mater Des 2019;164:107552. 107552.
[51] Costa MM, Lima R, Melo-Fonseca F, Bartolomeu F, Alves N, Miranda A, et al. Development of beta-TCP-Ti6Al4V structures: Driving cellular response by modulating physical and chemical properties. Mater. Sci. Eng. C Mater. Biol. Appl. 2019;98:705–16.
[52] Shi Q, Sun Y, Yang S, Van Dessel J, Lübbers H-T, Zhong S, et al. Failure analysis of an in-vivo fractured patient-specific Ti6Al4V mandible reconstruction plate fabricated by selective laser melting. Eng. Failure Anal. 2021;124.
[53] Prochor P, Mierzejewska ŻA. Bioactivity of PEEK GRF30 and Ti6Al4V SLM in simulated body fluid and Hank's Balanced Salt solution. Mater 2021;14:2059.
[54] Bsat S, Yavari SA, Munsch M, Valstar ER, Zadpoor AA. Effect of Alkali-acid-heat chemical surface treatment on electron beam melted porous titanium and its apatite forming ability. Mater 2015;8:1612–25.
[55] Ran Q, Yang W, Hu Y, Shen X, Yu Y, Xiang Y, et al. Osteogenesis of 3D printed porous Ti6Al4V implants with different pore sizes. J Mech Behav Biomed Mater 2018;84:1–11.
[56] Zhao B, Wang H, Qiao N, Wang C, Hu M. Corrosion resistance characteristics of a Ti-6Al-4V alloy scaffold that is fabricated by electron beam melting and selective laser melting for implantation in vivo. Mater. Sci. Eng. C Mater. Biol. Appl. 2017;70:832–41.
[57] Demirci S, Dalmış R, Dikici T, Tünçay MM, Kaya N, Güllüoğlu AN. Effect of surface modifications of additively manufactured Ti-6Al-4V alloys on apatite formation ability for biomedical applications. J Alloys Compd 2021:887.
[58] Liu H, Cui J, Bai X, Liu R, Yang D, Xu T, et al. Suppressing photocarrier recombination in anatase TiO2 nanoplates via thickness optimization for enhanced photocatalytical H2 generation. Appl Surf Sci 2021;566:150698.
[59] Zhao D, Han C, Li J, Liu J, Wei Q. In situ fabrication of a titanium-niobium alloy with tailored microstructures, enhanced mechanical properties and biocompatibility by using selective laser melting. Mater Sci Eng, C 2020;111:110784.
[60] Wang Q, Han C, Choma T, Wei Q, Yan C, Song B, et al. Effect of Nb content on microstructure, property and in vitro apatite-forming capability of Ti-Nb alloys fabricated via selective laser melting. Mater Des 2017;126:268–77.
[61] Abdel-Salam M, El-Hadad S, Khalifa W. Effects of microstructure and alloy composition on hydroxyapatite precipitation on alkaline treated α/β titanium alloys. Mater Sci Eng, C 2019;104:109974.
[62] Li L, Chen Y, Lu Y, Qin S, Huang G, Huang T, et al. Effect of heat treatment on the corrosion resistance of selective laser melted Ti6Al4V3Cu alloy. J Mater Res Technol 2021;12:904–15.